Models and methods for two-layer shallow water flows

Alexandre Chiapolino[1a,b], Richard Saurel[2a,b,c]

[a] *Aix Marseille Univ, CNRS, Centrale Marseille, LMA, Marseille, France*
[b] *RS2N, Chemin de Gaumin, Saint-Zacharie 83640, France*
[c] *IUF, University Institute of France*

Abstract

Two-layer shallow water models present at least two fundamental difficulties that are addressed in the present contribution. The first one is related to the lack of hyperbolicity of most existing models. By considering weak compressibility of the phases, a strictly hyperbolic formulation with pressure relaxation is obtained. It is shown to tend to the conventional two-layer model in the stiff pressure relaxation limit. The second issue is related to the non-conservative terms in the momentum equations. Analyzing the Riemann problem structure, local constants appear precisely at locations where the non-conservative products need definition. Thanks to these local constants, a locally conservative formulation of the equations is obtained, simplifying the Riemann problem resolution through a HLL-type Riemann solver. The method is compared to literature data, showing accurate and oscillation free solutions. Additional numerical experiments show robustness and accuracy of the method.

Keywords: multiphase flows, shallow water, hyperbolic systems, Riemann problem, non-conservative, relaxation.

[1]Corresponding author: alexandre.chiapolino@rs2n.eu
[2]richard.saurel@univ-amu.fr

1. Introduction

Two-layer (and multi-layer) shallow-water models are particularly useful in some limit cases of multi-fluid and variable density flows separated by nearly horizontal interfaces. These models govern the dynamics of incompressible fluids spreading under gravity effects. It can be for example:

- Flows of the same liquid but at different temperatures, resulting in differences in densities, such situation being typical of oceanic flows;
- Flows of two liquids of different densities;
- Flows of two gases evolving at low Mach number.

The two-layer approach is particularly interesting compared to multidimensional approaches, that consider vertical motion, as it enables much faster computations. It is also helpful when the height of one of the phases is arbitrarily small, as there is no need to spatially resolve it. Thereby, no numerical diffusion of the nearly horizontal interface is present and no interface tracking is needed. However, there are obviously some limitations with this approach:

- The vertical velocity component is neglected;
- The velocity and pressure are assumed uniform in cross sections of each layer.

Such type of modeling also involves serious difficulties. Indeed, most models are not hyperbolic, this issue having serious consequences both for propagation phenomenon, which becomes ill-posed, and for the design of numerical methods. A second serious difficulty appears as non-conservative terms are present in the momentum equations. The present paper addresses these two difficulties and provides solutions.

In the frame of averaged (or homogenized) equations in fluid mechanics, the issue related to the lack of hyperbolicity appears in different type of models, such as those of non-equilibrium two-phase flows (Marble (1963) [1], Baer and Nunziato (1986) [2], Saurel et al. (2017) [3]). There are mainly two types of remedy to cure this issue:

– Consider compressibility of the phases and deal with pressure relaxation [4]. This approach involves sound propagation in the phases and is particularly efficient in many situations. It has been adopted in the last two above-mentioned references.

– Consider turbulent effects in the phases, as they result in the appearance of a "turbulent sound speed" (Forestier et al. (1997) [5], Saurel et al. (2003) [6], Lhuillier et al. (2013) [7]). In the frame of shallow water flows, these effects have been studied in Richard and Gavrilyuk (2012) [8] and Gavrilyuk et al. (2016) [9].

In the present work, the first method is adopted and the fluids are considered weakly compressible. The resulting model is strictly hyperbolic and in the limit of stiff pressure relaxation, the conventional (non-hyperbolic) two-layer model is recovered. This approach is reminiscent of the model of Abgrall and Karni (2009) [10], except that extra pressure terms are present in the momentum equations of the new formulation. It also gives another interpretation of the relaxation approach, now based on compressibility and pressure effects.

The second issue is addressed as well and is related to the presence of non-conservative terms in the momentum equations. By examining the Riemann problem's structure, it appears that local constants are present, at locations where the derivative of the Heaviside function emerges. Consequently the non-conservative products become well defined. Also, local conservation laws are obtained and used in the frame of HLL-type Riemann solver.

The accuracy of the new solver is checked against results of Abgrall and Karni (2009) [10] as well as results obtained with a flow solver based on the VFRoe method of Gallouet and Masella (1996) [11] as it is able to deal, to some extent, with conservative and non-conservative models. The new method, based on HLL-type solver shows results of high accuracy and is oscillation free.

The paper is organized as follows. The two-layer hyperbolic model is presented in Section 2 and its stiff mechanical relaxation limit is examined. Both approximate VFRoe solver and non-conservative HLL solver are considered in Section 3. A Godunov-type scheme is derived in the same section. Results and validations are addressed in Sections 4 and 5. Conclusions are given in Section 6.

2. Hyperbolic two-layer shallow water model

The conventional two-layer shallow water model (Ovsyannikov (1979) [12]) reads,

$$\begin{cases} \dfrac{\partial(h_1\rho_1)}{\partial t} + \dfrac{\partial\left(h_1\rho_1 u_1\right)}{\partial x} = 0, \\ \dfrac{\partial\left(h_1\rho_1 u_1\right)}{\partial t} + \dfrac{\partial\left(h_1\rho_1 u_1^2 + \frac{1}{2}\rho_1 g h_1^2 + g\rho_2 h_1 h_2\right)}{\partial x} = \rho_2 g h_2 \dfrac{\partial h_1}{\partial x}, \\ \dfrac{\partial(h_2\rho_2)}{\partial t} + \dfrac{\partial\left(h_2\rho_2 u_2\right)}{\partial x} = 0, \\ \dfrac{\partial\left(h_2\rho_2 u_2\right)}{\partial t} + \dfrac{\partial\left(h_2\rho_2 u_2^2 + \frac{1}{2}\rho_2 g h_2^2\right)}{\partial x} = -\rho_2 g h_2 \dfrac{\partial h_1}{\partial x}. \end{cases} \tag{2.1}$$

h_1 and h_2 denote the heights of the two layers, ρ_1 and ρ_2 represent the densities of the fluids, considered constant at this level, u_1 and u_2 denote the fluids' velocities, averaged in each layer and g represents the gravity constant. Topography effects have been omitted for the sake of simplicity as well as friction with the bottom and between layers.

System (2.1) has been examined in Abgrall and Karni (2009) [10] and Monjarret (2015) [13] and appeared hyperbolic for small velocity drift only,

$$(u_1 - u_2)^2 < (h_1 + h_2) g (1 - \frac{\rho_2}{\rho_1}). \tag{2.2}$$

Moreover the waves' speeds can hardly be computed, rendering the system intricate to solve numerically. The pressure non-equilibrium formulation that follows addresses these modeling issues:

$$\begin{cases} \dfrac{\partial h_1}{\partial t} + u_1 \dfrac{\partial h_1}{\partial x} = \mu(p_1 - p_0), \\ \dfrac{\partial(h_1\rho_1)}{\partial t} + \dfrac{\partial\left(h_1\rho_1 u_1\right)}{\partial x} = 0, \\ \dfrac{\partial\left(h_1\rho_1 u_1\right)}{\partial t} + \dfrac{\partial\left(h_1\rho_1 u_1^2 + h_1 p_1(\rho_1) + \frac{1}{2}\rho_1 g h_1^2 + g\rho_2 h_1 h_2\right)}{\partial x} = \rho_2 g h_2 \dfrac{\partial h_1}{\partial x} + p_0 \dfrac{\partial h_1}{\partial x}, \\ \dfrac{\partial h_2}{\partial t} + u_2 \dfrac{\partial h_2}{\partial x} = \mu(p_2 - p_0), \\ \dfrac{\partial(h_2\rho_2)}{\partial t} + \dfrac{\partial\left(h_2\rho_2 u_2\right)}{\partial x} = 0, \\ \dfrac{\partial\left(h_2\rho_2 u_2\right)}{\partial t} + \dfrac{\partial\left(h_2\rho_2 u_2^2 + h_2 p_2(\rho_2) + \frac{1}{2}\rho_2 g h_2^2\right)}{\partial x} = -\rho_2 g h_2 \dfrac{\partial h_1}{\partial x} + p_0 \dfrac{\partial h_2}{\partial x}. \end{cases} \tag{2.3}$$

Two equations have been added and express the transport of the heights of the fluids' layers that are assumed to vary as a function of pressure differentials $(p_k - p_0)$. p_k denotes the thermodynamic pressure of fluid k, given by barotropic (and convex) equations of state $p_k(\rho_k)$. Example of such equation of state (EOS) is,

$$p_k(\rho_k) = p_k^{(0)} + c_k^{(0)^2}\left(\rho_k - \rho_k^{(0)}\right), \tag{2.4}$$

with $k = 1, 2$. Other options, such as Tait EOS for instance are possible. We will see that the choice of the EOS is not important, only the related sound speed $c_k^{(0)}$ has importance. p_0 denotes the (constant) atmospheric pressure and $p_k^{(0)} = p_0$.

The pressure relaxation parameter μ is related to the fluids' sound speeds and heights of layers. It controls the rate at which pressure equilibrium is reached. Following Saurel et al. (2017) [3], the first equation of System (2.3) can be written as,

$$\frac{d_1 h_1}{dt} = \frac{h_1}{\tau}\frac{p_1 - p_0}{\rho_1 c_1^2},$$

where $\frac{d_1}{dt} = \frac{\partial}{\partial t} + u_1\frac{\partial}{\partial x}$ and τ is the pressure relaxation time,

$$\tau = \frac{h_1}{c_1}. \tag{2.5}$$

In most situations, this relaxation time is on the order of $\frac{1}{100}$ second, meaning that the relaxation parameter μ is large ($\mu \simeq \text{Max}\left(\tau_1^{-1}, \tau_2^{-1}\right)$). In practical computations, the relaxation time τ will be assumed of the same order as the computational time step and stiff pressure relaxation will be done at the end of each time step. Therefore, there is no need of precise knowledge of the pressure relaxation parameter μ.

This system is reminiscent of Baer and Nunziato's (1986) [2] model widely used in two-phase flow modeling. It is also reminiscent of Abgrall and Karni's (2009) [10] relaxation model, except that pressure terms have been added to the momentum equations ($h_1 p_1(\rho_1)$ and $h_2 p_2(\rho_2)$). To maintain mechanical equilibrium, extra non-conservative terms have been added in the right-hand side ($p_0\frac{\partial h_k}{\partial x}$). Let us now examine some relevant properties to check validity of this formulation.

2.1. Hyperbolicity

System (2.3) is expressed in primitive-variable formulation (without source terms) as,

$$\frac{\partial W}{\partial t} + A(W)\frac{\partial W}{\partial x} = 0, \tag{2.6}$$

with,

$$W = \begin{pmatrix} h_1 \\ \rho_1 \\ u_1 \\ h_2 \\ \rho_2 \\ u_2 \end{pmatrix}, \quad A(W) = \begin{pmatrix} u_1 & 0 & 0 & 0 & 0 & 0 \\ 0 & u_1 & \rho_1 & 0 & 0 & 0 \\ \frac{p_1-p_0}{h_1\rho_1} + g & \frac{c_1^2+\frac{1}{2}gh_1}{\rho_1} & u_1 & g\frac{\rho_2}{\rho_1} & \frac{gh_2}{\rho_1} & 0 \\ 0 & 0 & 0 & u_2 & 0 & 0 \\ 0 & 0 & 0 & 0 & u_2 & \rho_2 \\ g & 0 & 0 & \frac{p_2-p_0}{h_2\rho_2} + g & \frac{c_2^2+\frac{1}{2}gh_2}{\rho_2} & u_2 \end{pmatrix}. \tag{2.7}$$

The waves' speeds are solution of $\det\left(A(W) - \lambda \underline{\underline{I}}\right) = 0$ resulting in,

$$(u_1-\lambda)(u_2-\lambda)\left[(u_2-\lambda)^2 - \left(c_2^2 + \frac{1}{2}gh_2\right)\right]\left[(u_1-\lambda)^2 - \left(c_1^2 + \frac{1}{2}gh_1\right)\right] = 0. \tag{2.8}$$

Six real and distinct eigenvalues appear as:

$$\begin{cases} \lambda_1 = u_1, \quad \lambda_2 = u_1 + \sqrt{c_1^2 + \frac{1}{2}gh_1}, \quad \lambda_3 = u_1 - \sqrt{c_1^2 + \frac{1}{2}gh_1}, \\ \lambda_4 = u_2, \quad \lambda_5 = u_2 + \sqrt{c_2^2 + \frac{1}{2}gh_2}, \quad \lambda_6 = u_2 - \sqrt{c_2^2 + \frac{1}{2}gh_2}. \end{cases} \tag{2.9}$$

Those eigenvalues correspond to the waves' speeds emerging at a given initial discontinuity, as schematized in Fig. 1.

System (2.3) is consequently strictly hyperbolic. This model is however relevant with respect to the physics expressed in (2.1) if it tends to the same equations when pressure relaxation is stiff. This limit is examined hereafter.

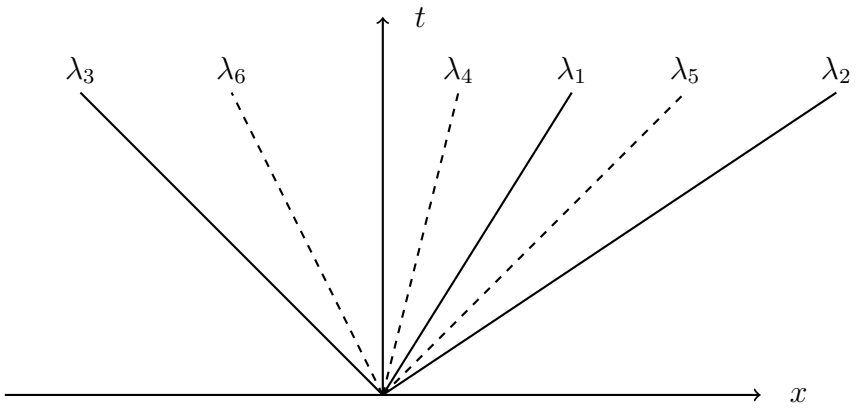

Figure 1: Schematic representation in the (x,t) diagram of the six waves (2.9) present in the flow model (2.3) and emerging at a given initial discontinuity.

2.2. Stiff pressure relaxation limit

The mass and height equations of a given phase are analyzed:

$$\begin{cases} \dfrac{\partial h_k}{\partial t} + u_k \dfrac{\partial h_k}{\partial x} = \mu(p_k - p_0), \\ \dfrac{\partial (h_k \rho_k)}{\partial t} + \dfrac{\partial \left(h_k \rho_k u_k\right)}{\partial x} = 0, \end{cases}$$

with $k = 1, 2$. Their combination results in,

$$\frac{d_k \rho_k}{dt} + \rho_k \frac{\partial u_k}{\partial x} = -\frac{\rho_k}{h_k} \mu \left(p_k - p_0\right).$$

Inserting the phase k equation of state $p_k(\rho_k)$, the following pressure evolution equation is obtained,

$$\frac{d_k p_k}{dt} + \rho_k c_k^2 \frac{\partial u_k}{\partial x} = -\frac{\rho_k c_k^2}{h_k} \mu \left(p_k - p_0\right).$$

As the atmospheric pressure p_0 is constant, the last equation can be expressed as,

$$\frac{d_k (p_k - p_0)}{dt} + \rho_k c_k^2 \frac{\partial u_k}{\partial x} = -\frac{\rho_k c_k^2}{h_k} \mu \left(p_k - p_0\right).$$

The phase pressure is expressed around the equilibrium state with the following expansion,

$$p_k = \rho_k c_k^2 \left(p_k^{(0)} + \epsilon p_k^{(1)} + \ldots\right),$$

where

- ϵ is on the order of the inverse of pressure relaxation parameter ($\epsilon \simeq \mu^{-1} \simeq \tau$), tending to zero in most situations ($\epsilon \to 0^+$) as discussed earlier (see also Kapila et al. (2001) [14] for estimates in the context of granular flows),
- $p_k^{(0)}$ and $p_k^{(1)}$ represent respectively the leading and first-order dimensionless pressure terms of the Taylor expansion.

Inserting these definitions in the pressure evolution equation,

$$\frac{d_k\left(\rho_k c_k^2\left[p_k^{(0)} + \epsilon p_k^{(1)} + \dots\right] - p_0\right)}{dt} + \rho_k c_k^2 \frac{\partial u_k}{\partial x} = -\frac{\rho_k c_k^2}{h_k}\frac{1}{\epsilon}\left(\rho_k c_k^2\left[p_k^{(0)} + \epsilon p_k^{(1)} + \dots\right] - p_0\right),$$

the following results are obtained:

- At leading order (ϵ^{-1}): $p_k^{(0)} = p_0$;
- At first order $\rho_k c_k^2 p_k^{(1)} = -h_k \frac{\partial u_k}{\partial x}$.

Inserting this last result in the height equations, they become,

$$\frac{\partial h_k}{\partial t} + \frac{\partial\left(h_k u_k\right)}{\partial x} = 0.$$

The mass equations are unchanged while modifications in the momentum equations appear as a consequence of the equilibrium condition ($p_k = p_0$). They finally result at leading order in,

$$\begin{cases} \dfrac{\partial\left(h_1\rho_1 u_1\right)}{\partial t} + \dfrac{\partial\left(h_1\rho_1 u_1^2 + \frac{1}{2}\rho_1 g h_1^2 + g\rho_2 h_1 h_2\right)}{\partial x} = \rho_2 g h_2 \dfrac{\partial h_1}{\partial x}, \\ \dfrac{\partial\left(h_2\rho_2 u_2\right)}{\partial t} + \dfrac{\partial\left(h_2\rho_2 u_2^2 + \frac{1}{2}\rho_2 g h_2^2\right)}{\partial x} = -\rho_2 g h_2 \dfrac{\partial h_1}{\partial x}. \end{cases}$$

System (2.1) is recovered, complemented by two conservation equations for the heights, that are in agreement with the two mass equations as soon as the densities are constants.

It thus appears that System (2.3) tends to System (2.1) when pressure relaxation is stiff. As System (2.3) is hyperbolic, it is a good candidate to approximate (2.1) numerically with a two-step procedure:

– Solve the hyperbolic system (2.3) without source terms;

– Relax the pressures onto the atmospheric one and reset the heights.

This is similar to the method of Saurel and Abgrall (1999) [15] to compute flows with interfaces separating two fluids. Before entering in the details of the hyperbolic solver, let us present the pressure relaxation process, that is particularly simple in the present context.

2.3. Stiff pressure relaxation solver

Let us consider for example EOS (2.4). Consequently, the densities as functions of pressures are given by:

$$\rho_k = \rho_k^{(0)} + \frac{p_k - p_k^{(0)}}{c_k^{(0)^2}}. \tag{2.10}$$

As the pressures relax to the atmospheric one ($p_k = p_k^{(0)} = p_0$), the densities at relaxed pressure are just,

$$\rho_k^* = \rho_k^{(0)}, \tag{2.11}$$

where the superscript * denotes the relaxed pressure state. As the masses of each layer are computed by associated mass balance equations and are constant during the relaxation process,

$$m_k = h_k \rho_k = h_k^* \rho_k^*, \tag{2.12}$$

the heights at relaxed states are reset as,

$$h_k^* = \frac{h_k \rho_k}{\rho_k^{(0)}}. \tag{2.13}$$

The stiff pressure relaxation solver just consists in the reset of the heights of the fluids $h_k \to h_k^*$. At this level, the relaxation method of Abgrall and Karni (2009) [10] is recovered. We now address the design of hyperbolic solvers.

3. Approximate Riemann solvers

Two different approximate methods are considered to solve the Riemann problem of System (2.3), the VFRoe method (Gallouet and Masella (1996) [11]) and a new HLL-type Riemann solver (Harten et al. (1983) [16]). As System (2.3) contains non-conservative terms, an approach dealing with both conservative and non-conservative systems is examined first.

3.1. VFRoe solver

The VFRoe method considers the equations in non-conservative formulation,

$$\frac{\partial W}{\partial t} + A(\overline{W})\frac{\partial W}{\partial x} = 0, \tag{3.1}$$

with

$$W = (h_1,\ \rho_1,\ u_1,\ h_2,\ \rho_2,\ u_2)^T \quad \text{and} \quad \overline{W} = \frac{W_L + W_R}{2},$$

where W_L and W_R are respectively the left and right-state vectors at a given cell boundary.

The VFRoe method considers the exact Riemann problem solution of (3.1). Note that (3.1) is a local linearization of the non-linear flow model (2.3) around state $\overline{W}$. The VFRoe solution is thus the exact solution of an approximate problem.

The exact solution of (3.1) may be found in many textbooks related to hyperbolic systems (LeVeque (2002) [17], Toro (2013) [18]) and can be summarized as follows,

$$W^* = W_L + \sum_{\overline{\lambda_i}<0} \overline{a_i}\overline{R_i} = W_R - \sum_{\overline{\lambda_i}>0} \overline{a_i}\overline{R_i}, \tag{3.2}$$

where the wave strengths $\overline{a_i}$ are the coefficients of the eigenvectors' decomposition,

$$W_R - W_L = \sum_{\overline{\lambda_i}} \overline{a_i}\overline{R_i}. \tag{3.3}$$

For the sake of space restriction, the right eigenvectors R_i and the wave strengths $\overline{a_i}$ are not detailed, associated formulas being considerably large. The main weakness of this method is related to the average $\overline{W}$ which can be far from the solution of the non-linear problem, resulting in positivity issues especially when large amplitude waves are present.

With the help of the Riemann problem solution (3.2), the various equations of System (2.3) are updated with a Godunov-type method (stable under the conventional CFL condition) as,

$$h_k^{n+1} = h_k^n - \frac{\Delta t}{\Delta x}\left((hu)^*_{k,i+\frac{1}{2}} - (hu)^*_{k,i-\frac{1}{2}}\right) + \frac{\Delta t}{\Delta x} h^n_{k,i}\left(u^*_{k,i+\frac{1}{2}} - u^*_{k,i-\frac{1}{2}}\right), \tag{3.4}$$

$$(h_k\rho_k)_i^{n+1} = (h_k\rho_k)_i^n - \frac{\Delta t}{\Delta x}\left((h_k\rho_k u_k)^*_{i+\frac{1}{2},\,k} - (h_k\rho_k u_k)^*_{i-\frac{1}{2},\,k}\right), \tag{3.5}$$

$$\begin{aligned}(h_1\rho_1 u_1)_i^{n+1} = (h_1\rho_1 u_1)_i^n - \frac{\Delta t}{\Delta x}\Bigg\{ &\left(h_1\rho_1 u_1^2 + h_1(p_1 - p_0) + \frac{1}{2}\rho_1 h_1^2\right)^*_{i+\frac{1}{2}} \\ &- \left(h_1\rho_1 u_1^2 + h_1(p_1 - p_0) + \frac{1}{2}\rho_1 h_1^2\right)^*_{i-\frac{1}{2}} \Bigg\} + \frac{\Delta t}{\Delta x} h^n_{1,i}\Big\{(-\rho_2 g h_2)^*_{i+\frac{1}{2}} - (-\rho_2 g h_2)^*_{i-\frac{1}{2}}\Big\},\end{aligned} \tag{3.6}$$

$$\begin{aligned}(h_2\rho_2 u_2)_i^{n+1} = (h_2\rho_2 u_2)_i^n - \frac{\Delta t}{\Delta x}\Bigg\{ &\left(h_2\rho_2 u_2^2 + h_2(p_2 - p_0) + \frac{1}{2}\rho_2 h_2^2 + \rho_2 g h_1 h_2\right)^*_{i+\frac{1}{2}} \\ &- \left(h_2\rho_2 u_2^2 + h_2(p_2 - p_0) + \frac{1}{2}\rho_2 h_2^2 + \rho_2 g h_1 h_2\right)^*_{i-\frac{1}{2}} \Bigg\} \\ &+ \frac{\Delta t}{\Delta x} h^n_{1,i}\Big\{\left((\rho_2 g h_2)^*_{i+\frac{1}{2}} - (\rho_2 g h_2)^*_{i-\frac{1}{2}}\right)\Big\},\end{aligned} \tag{3.7}$$

where $n+1$ and n denote two consecutive time steps and superscript * denotes the VFRoe Riemann problem solution given by Eq. (3.2). Indexes i and $i \pm \frac{1}{2}$ denote respectively the center of the current numerical cell and its corresponding boundaries.

3.2. HLL-type Riemann solver

Let us consider a simplified solver, based on Rankine-Hugoniot conditions, such as the HLL solver. In this frame, the two extreme waves S_L and S_R are approximated following Davis (1988) [19] as,

$$\begin{cases} S_{L,k} = \min\left(u_{L,k} - \sqrt{c^2_{L,k} + \frac{1}{2} g h_{L,k}}\ \ ,\ \ u_{R,k} - \sqrt{c^2_{R,k} + \frac{1}{2} g h_{R,k}}\right), \\ S_{R,k} = \max\left(u_{L,k} + \sqrt{c^2_{L,k} + \frac{1}{2} g h_{L,k}}\ \ ,\ \ u_{R,k} + \sqrt{c^2_{R,k} + \frac{1}{2} g h_{R,k}}\right), \end{cases} \tag{3.8}$$

with $k = 1, 2$. The indexes $_L$ and $_R$ denote respectively the left and right states at a given cell boundary. The two extreme waves are considered as,

$$S_L = \min\left(S_{L,1}, S_{L,2}\right), \quad S_R = \max\left(S_{R,1}, S_{R,2}\right). \tag{3.9}$$

The two contact waves u_1 and u_2 are considered as well for the transport of the heights h_1 and h_2, as depicted in Fig 2.

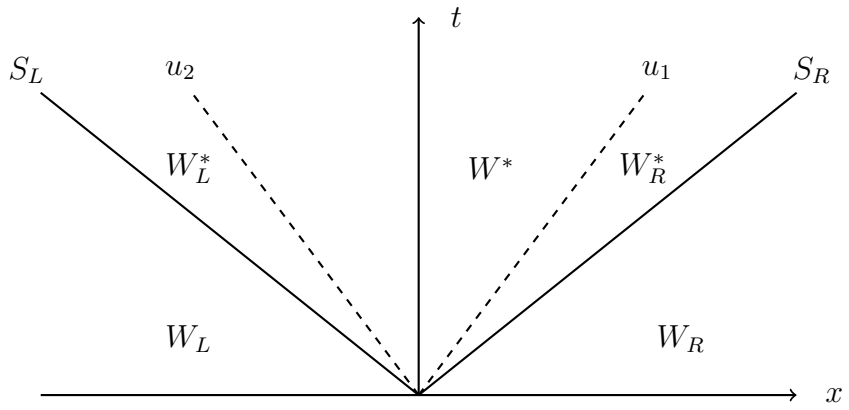

Figure 2: Schematic representation in the (x,t) diagram of the two extreme waves and the two contact waves considered for the transport of the two heights.

Regarding the transport equations, the exact Riemann problem solution is straightforward:

$$\begin{cases} h_1^*\left(\dfrac{x}{t} < u_1^*\right) = h_{1,L}, & h_1^*\left(\dfrac{x}{t} > u_1^*\right) = h_{1,R}, \\ h_2^*\left(\dfrac{x}{t} < u_2^*\right) = h_{2,L}, & h_2^*\left(\dfrac{x}{t} > u_2^*\right) = h_{2,R}. \end{cases} \tag{3.10}$$

These solutions indicate that the non-conservative terms have contributions between the two extreme waves S_R and S_L, at points where h_1 and h_2 are discontinuous. More precisely, only the discontinuity in h_1 needs attention, as the non-conservative terms involving the atmospheric pressure (considered constant) transform to fluxes,

$$p_0 \frac{\partial h_k}{\partial x} = \frac{\partial (p_0 h_k)}{\partial x}.$$

It thus remains to analyze only the non-conservative term,

$$\rho_2 g h_2 \frac{\partial h_1}{\partial x}.$$

The solution states for $(\rho_2 h_2)$ are given by,

$$(\rho_2 h_2)^*_L = (\rho_2 h_2)_L \frac{u_{2,L} - S_L}{u^*_2 - S_L} \quad \text{and} \quad (\rho_2 h_2)^*_R = (\rho_2 h_2)_R \frac{u_{2,R} - S_R}{u^*_2 - S_R}.$$

A schematic representation is given in Fig.3.

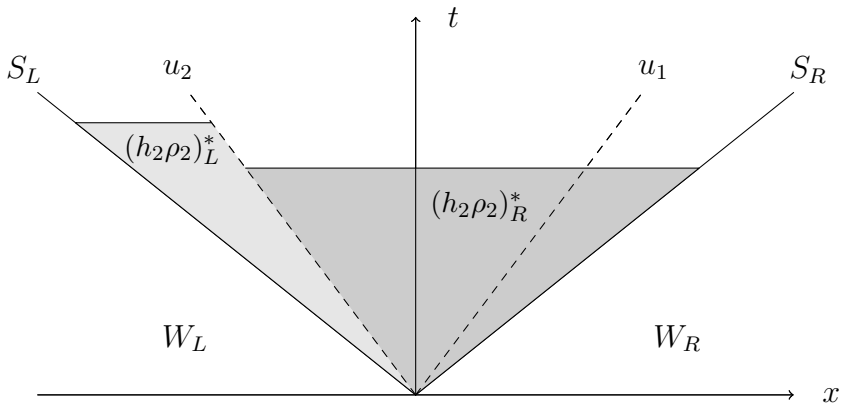

Figure 3: Schematic representation in the (x,t) diagram of the two levels $(\rho_2 h_2)^*_{L,R}$ in the Riemann problem solution.

These formulas need u^*_2 for their practical use that is unknown at this level. However, according to the sign of the velocity difference $u^*_1 - u^*_2$, only two instances may occur:

– If $u^*_1 > u^*_2$, the $\rho_2 g h_2 \frac{\partial h_1}{\partial x}$ term becomes locally $g\,(\rho_2 h_2)^*_R \frac{\partial h_1}{\partial x}$. As $(\rho_2 h_2)^*_R$ is constant at the point where $\frac{\partial h_1}{\partial x}$ is discontinuous, the non-conservative term becomes locally;

$$\rho_2 g h_2 \frac{\partial h_1}{\partial x} = \frac{\partial \left[g\,(\rho_2 h_2)^*_R\, h_1 \right]}{\partial x}.$$

– If $u^*_1 < u^*_2$, the same reasoning yields,

$$\rho_2 g h_2 \frac{\partial h_1}{\partial x} = \frac{\partial \left[g\,(\rho_2 h_2)^*_L\, h_1 \right]}{\partial x}.$$

It thus appears that the momentum equations are locally conservative. However, their explicit determination and use require knowledge of both u^*_1 and u^*_2 that are themselves solutions of the momentum equations' integration.

To simplify the algorithm, a single solution state is considered for the apparent densities $(\rho_k h_k)^*$ instead of the two $(\rho_k h_k)^*_L$ and $(\rho_k h_k)^*_R$ in the same mind as in the HLL solver for the Euler equations:

$$(h_k\rho_k)^* = \frac{(h_k\rho_k)_R(u_{k,R} - S_R) - (h_k\rho_k)_L(u_{kL} - S_L)}{S_L - S_R}. \tag{3.11}$$

Thanks to this approximation, the momentum equations become locally,

$$\begin{cases} \dfrac{\partial\left(h_1\rho_1 u_1\right)}{\partial t} + \dfrac{\partial\left(h_1\rho_1 u_1^2 + h_1\big[p_1(\rho_1) - p_0\big] + \frac{1}{2}\rho_1 g h_1^2 + g\rho_2 h_1 h_2 - g(h_2\rho_2)^* h_1\right)}{\partial x} = 0, \\ \dfrac{\partial(h_2\rho_2 u_2)}{\partial t} + \dfrac{\partial\left(h_2\rho_2 u_2^2 + h_2\big[p_2(\rho_2) - p_0\big] + \frac{1}{2}\rho_2 g h_2^2 + g(h_2\rho_2)^* h_1\right)}{\partial x} = 0. \end{cases} \tag{3.12}$$

Denoting the momentum fluxes by,

$$\begin{cases} F_{1,mom} = h_1\rho_1 u_1^2 + h_1\big[p_1(\rho_1) - p_0\big] + \dfrac{1}{2}\rho_1 g h_1^2 + g\rho_2 h_1 h_2 - g(h_2\rho_2)^* h_1, \\ F_{2,mom} = h_2\rho_2 u_2^2 + h_2\big[p_2(\rho_2) - p_0\big] + \dfrac{1}{2}\rho_2 g h_2^2 + g(h_2\rho_2)^* h_1, \end{cases} \tag{3.13}$$

the momentum numerical fluxes are then given by,

$$F^*_{k,mom} = \frac{F_{k,mom,R}S_L - F_{k,mom,L}S_R + S_L S_R(U_{k,mom,L} - U_{k,mom,R})}{S_L - S_R}, \tag{3.14}$$

with $U_{k,mom} = h_k\rho_k u_k$. The mass numerical fluxes are computed by the HLL approximation as well and read,

$$F^*_{k,mass} = \frac{(h_k\rho_k)_R S_L(u_{k,R} - S_R) - (h_k\rho_k)_L S_R(u_{k,L} - S_L)}{S_L - S_R}. \tag{3.15}$$

System (2.1) being non-conservative, the conservative variable-state vector and in particular the fluids' velocities are also needed for the computations. With the help of Eqs. (3.12) and (3.13), the momentum variables are computed with the HLL approximation as,

$$(h_k\rho_k u_k)^* = \frac{F_{k,mom,R} - F_{k,mom,L} - S_R U_{k,mom,R} + S_L U_{k,mom,L}}{S_L - S_R}. \tag{3.16}$$

Using Eqs. (3.11) and (3.16), the speeds of the fluids are given by,

$$u_k^* = \frac{(h_k\rho_k u_k)^*}{(h_k\rho_k)^*}. \tag{3.17}$$

The associated Godunov-type method now reads,

$$\begin{cases} h_k^{n+1} = h_k^n - \dfrac{\Delta t}{\Delta x}\left((hu)^*_{k,i+\frac{1}{2}} - (hu)^*_{k,i-\frac{1}{2}}\right) + \dfrac{\Delta t}{\Delta x} h^n_{k,i}\left(u^*_{k,i+\frac{1}{2}} - u^*_{k,i-\frac{1}{2}}\right), \\ (h_k\rho_k)_i^{n+1} = (h_k\rho_k)_i^n - \dfrac{\Delta t}{\Delta x}\left(F^*_{k,mass,i+\frac{1}{2}} - F^*_{k,mass,i-\frac{1}{2}}\right), \\ (h_1\rho_1 u_1)_i^{n+1} = (h_1\rho_1 u_1)_i^n - \dfrac{\Delta t}{\Delta x}\left(F^*_{1,mom,i+\frac{1}{2}} - F^*_{1,mom,i-\frac{1}{2}}\right) + \dfrac{\Delta t}{\Delta x} h^n_{1,i}\left(-g\left[(h_2\rho_2)^*_{i+\frac{1}{2}} - (h_2\rho_2)^*_{i-\frac{1}{2}}\right]\right), \\ (h_2\rho_2 u_2)_i^{n+1} = (h_2\rho_2 u_2)_i^n - \dfrac{\Delta t}{\Delta x}\left(F^*_{2,mom,i+\frac{1}{2}} - F^*_{2,mom,i-\frac{1}{2}}\right) + \dfrac{\Delta t}{\Delta x} h^n_{1,i}\left(g\left[(h_2\rho_2)^*_{i+\frac{1}{2}} - (h_2\rho_2)^*_{i-\frac{1}{2}}\right]\right). \end{cases} \tag{3.18}$$

Efficiency of both VFRoe and HLL solvers are now investigated on various test problems of the literature.

4. Results and validations

It is important to address in priority the effects of the fluids' EOS with the present relaxation approach. Indeed the model is hyperbolic as a consequence of pressure terms in the momentum equations. Extra tests, where VFRoe and HLL solvers are compared are addressed subsequently.

4.1. Effects of the artificial sound speed

The EOS (2.4) involves a sound speed c_k that has influence on computed results, as shown hereafter in Figs. 4, 5 and 6. The examined configuration consists in a limit case where the initial height of the first fluid (lower layer) is as low as numerically admissible, so that only the upper layer (second fluid) evolves significantly. With this specific configuration, the solution of the two layer shallow water system (2.3) is meant to be compared to the exact solution of the one-layer Saint-Venant equations.

A dam-break problem is used to this end. The following test is proposed in LeVeque's textbook (2002) [17] to illustrate behavior of the solution of the Saint-Venant equations. It consists in a dam, separating two levels of fluids, that bursts at time $t = 0$. All variables of the

current test problem are in dimensionless units as done in [17]. This test is the shallow-water equivalent of the shock-tube problem of gas dynamics and appears to be an excellent benchmark as the flow deals with shock and expansion waves that create arduous conditions. The constant gravity is normalized and reads $g = 1$. The numerical domain has a length set to 10 with a height discontinuity initially located in the middle. On the left of this discontinuity, the fluid is initially at $h = 3$ and $h = 1$ on the right. The fluid is initially at rest on either side of the discontinuity.

To mimic the Saint-Venant system with the two-layer model (2.3), the height of the first fluid is initially set to $h_1 = \epsilon = 10^{-6}$ throughout the whole numerical domain. Its density is set to $\rho_1 = 1.2$ and its velocity is set to $u_1 = 0$. The second fluid, placed above the first one, has initial heights $h_2 = 3$ at left and $h_2 = 1$ at right. Its density is set to $\rho_2 = 1$ and its velocity is set to $u_2 = 0$.

Figure 4 shows the results with a constant sound speed set to $c_k = 100$. The same sound speed has been taken for both fluids for the sake of simplicity in this illustration. Also, two mesh resolutions are used in Fig. 4, a coarse one made of 100 cells (A) and a fine one made of $10,000$ cells (B).

It appears that the speed of sound influences computed results. The waves' speeds of the two-layer model (2.3) involve the effective sound speeds given by $\sqrt{c_k^2 + \frac{1}{2}gh_k}$ while the single layer wave speed is $\sqrt{gh}$. When c_k is significantly greater than $\sqrt{\frac{1}{2}gh_k}$ (of the order of unity in the present example), excessive numerical diffusion is present, as shown in Plot A of Fig. 4 where $c_k = 100$ for both fluids. Indeed, at the current time, the left and right facing waves are considerably dissipated and even exit the domain. However, this feature is purely numerical and the system does converge to the exact solution, as shown in Plot B of Fig. 4 that uses a fine grid made of $10,000$ cells.

It thus appears that large sound speeds are admissible but result in excessive numerical diffusion. The effect of fluid compressibility and sound speed are then investigated by varying c_k from levels less than the admissible single phase bound ($c_k < \sqrt{\frac{1}{2}gh_k}$) to larger values. Corresponding results are shown in Fig. 5.

Numerical experiments of Fig. 5 indicate that the method becomes unstable when $c_k <$

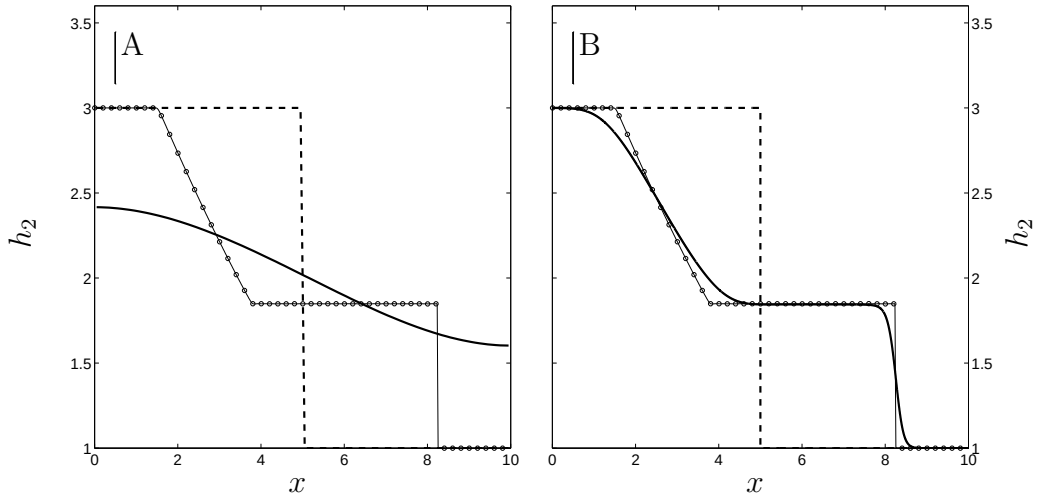

Figure 4: Comparison of the computed solutions with the present HLL-type Riemann solver (thick lines) versus the exact solution of the one-layer Saint-Venant equations (thin lines and symbols). Results on the left (A) use a 100-cell mesh while results on the right (B) use a $10,000$-cell mesh. The two plots use a constant sound speed set to $c_k = 100$ for both fluids. The dashed lines represent the initial conditions. For the sake of clarity, 50 symbols are plotted for the exact solution, shown at time $t \approx 2$. First-order Godunov-type numerical scheme is used with $CFL = 0.9$. Computed results are shown at the same time in full lines. Results at left (A) show a curved line where the shock and expansion waves have already exited the domain. Same computation is rerun with $10,000$ cells (B) restoring the two waves inside the domain. All variables are in dimensionless units.

$\sqrt{\frac{1}{2}gh_k}$. Indeed, Plot C of Fig. 5 uses $c_k = 0.1 \times \sqrt{\frac{1}{2}gh_k}$ and presents spurious oscillations. These numerical experiments suggest existence of a subcharacteristic condition:

$$c_k > \sqrt{\frac{1}{2}gh_k}. \tag{4.1}$$

In the upcoming computations, the following sound speed is used:

$$c_k = \theta_k \sqrt{\frac{1}{2}gh_k}, \quad \text{with} \quad \theta_k > 1, \quad k = 1, 2. \tag{4.2}$$

θ_k is a numerical parameter that controls the numerical diffusion as illustrated in Figure 5.

In order to unambiguously fulfill the above-mentioned subcharacteristic condition (4.1), θ_k must be greater than unit. $\theta_k \in [2\,,5]$ seems a fair choice as it is low enough to control numerical diffusion and high enough to ensure stability. Indeed, as seen in Plot D of Fig.5, $\theta_k = 2$ provides accurate results whereas $\theta_k = 10$ (Plot E) and $\theta_k = 50$ (Plot F) show excessive numerical dissipation.

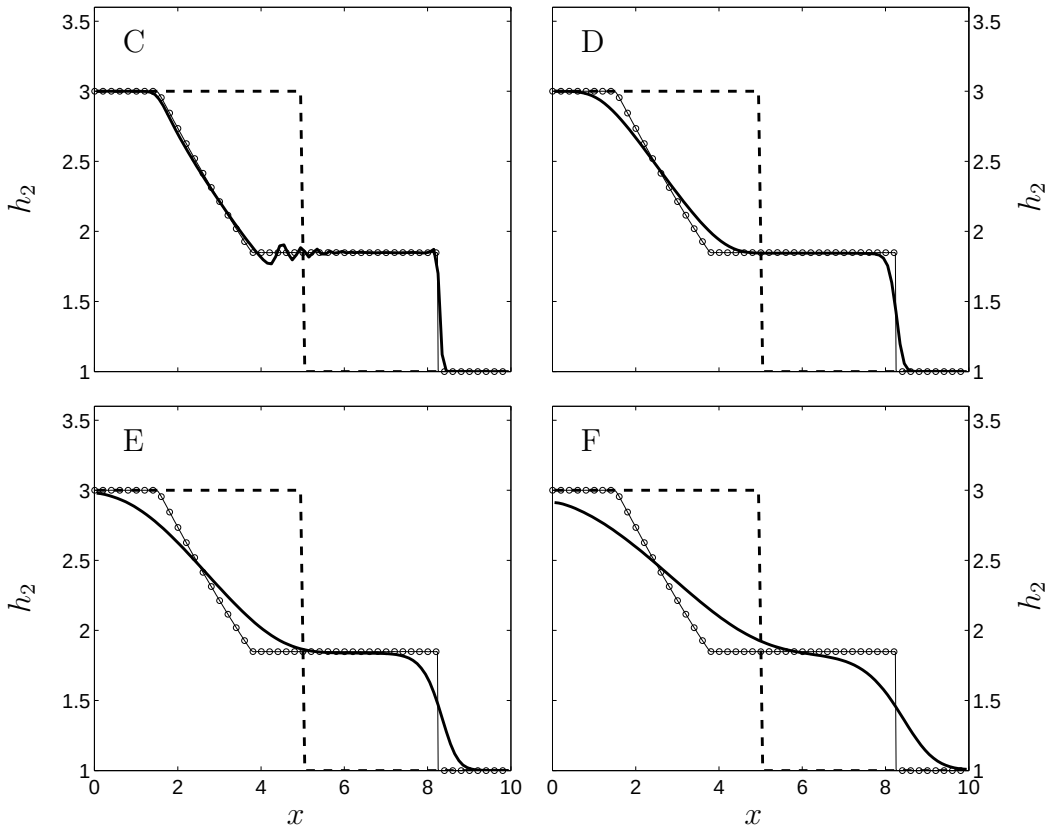

Figure 5: Comparison of the computed solutions with the present HLL-type Riemann solver (thick lines) for the two-layer model versus the exact solution of the one-layer Saint-Venant equations (thin lines and symbols). System (2.3) is solved with various sound speeds $c_k = \theta_k \sqrt{\frac{1}{2} g h_k}$. Figures C, D, E and F use respectively $\theta_k = 0.1$, $\theta_k = 2$, $\theta_k = 10$ and $\theta_k = 50$. The dashed lines represent the initial conditions: $h_1^{left} = h_1^{right} = 10^{-6}$, $u_1^{left} = u_1^{right} = 0$, $\rho_1 = 1.2$, $h_2^{left} = 3$, $h_2^{right} = 1$, $u_2^{left} = u_2^{right} = 0$, $\rho_2 = 1$. Final time: $t \approx 2$. All results use a 100-cell mesh. First-order Godunov-type numerical scheme is used with $CFL = 0.9$. For the sake of clarity, 50 symbols are plotted for the exact solution. An optimum appears for $\theta_k \simeq 2$. All variables are in dimensionless units.

Figure 6 repeats the same test with $\theta_k = 2$ and a 1000-cell grid. The Godunov method (3.18) including non-conservation terms is extended to second order with the MUSCL-type method detailed for example in Chiapolino et al. (2017) [20].

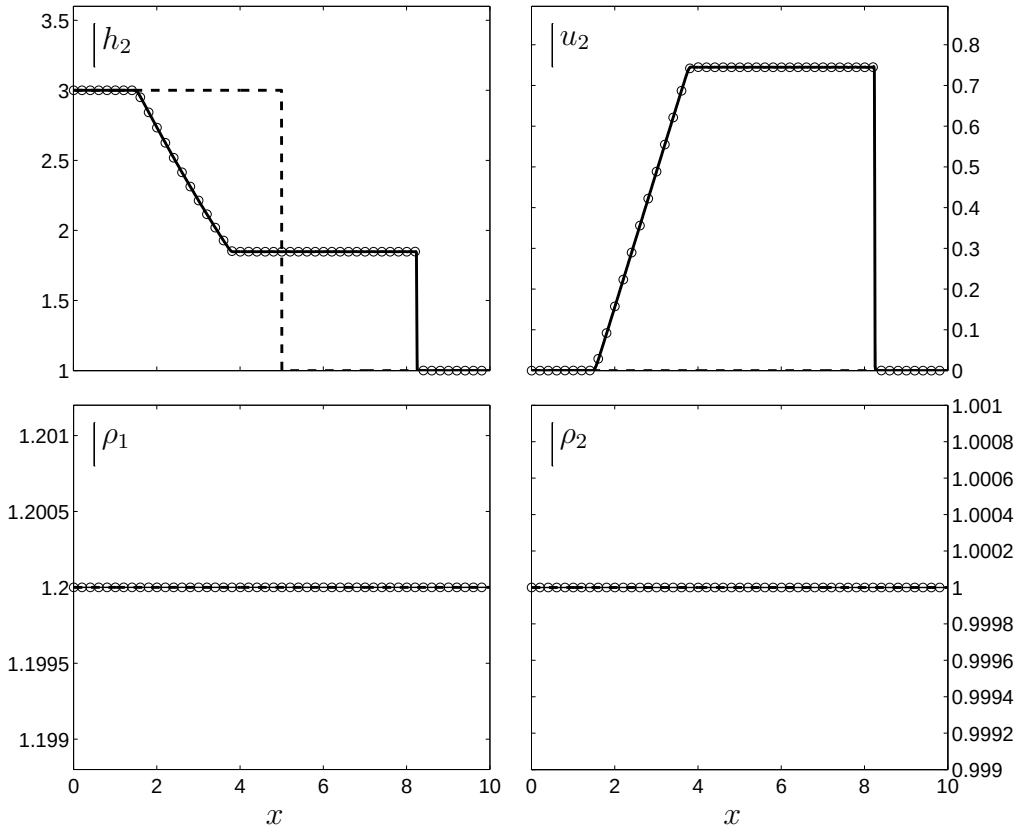

Figure 6: Comparison of the computed solutions with the present HLL-type Riemann solver (symbols) versus the exact solution of the one-layer Saint-Venant equations (thick lines). The numerical system uses an artificial sound speed reading $c_k = \theta_k \sqrt{\frac{1}{2} g h_k}$ with $\theta_k = 2$. The dashed lines represent the initial conditions: $h_1^{left} = h_1^{right} = 10^{-6}$, $u_1^{left} = u_1^{right} = 0$, $\rho_1 = 1.2$, $h_2^{left} = 3$, $h_2^{right} = 1$, $u_2^{left} = u_2^{right} = 0$, $\rho_2 = 1$. Final time: $t \approx 2$. Second-order MUSCL-type numerical scheme using van Leer's limiter (see [21], [22]) is considered with $CFL = 0.5$ and 1000 cells. For the sake of clarity, only 50 symbols out of 1000 are plotted for the HLL-type computations. All variables are in dimensionless units.

The results show excellent agreement with the exact solution. Besides, they also reveal that:

– Incompressible behavior is recovered as the densities ρ_k are constant;

– The two-layer shallow water model (2.3) tends to the single-layer Saint-Venant equations in the limit $h_1 \to \epsilon$;

– Second-order extension of the Godunov-type scheme (3.18) and associated non-conservative terms does not pose specific difficulties.

These various computations have been done with the HLL solver while the VFRoe one failed immediately, as it was unable to preserve positivity of the height h_1. It is also important to note that the method does not require any fluid EOS, nor relaxation parameter, as Eq. (2.13) determines efficiently the heights at relaxed states. The only "thermodynamic" information is the sound speed, and more precisely θ_k in Eq. 4.2. The method is robust and accurate with $2 \leq \theta_k \leq 5$.

4.2. Effects of the fluids' densities

The preceding dam-break problem showed that the two-layer shallow water model (2.3) is able to recover the single-layer Saint-Venant system in the limit $h_1 \to 0$. When the density ratio $r = \frac{\rho_2}{\rho_1}$ is small, the effects of the surrounding fluid (upper layer) are expected to become insignificant and the one-layer Saint-Venant solution is meant to be recovered as well.

The forthcoming tests analyze the effects of the fluids' densities on a configuration presenting initially a Heaviside function regarding the height of the first fluid (lower layer) located in the middle of the numerical domain. The first layer is initially at height h_1 above the flat ground and the top of the plateau is located at height h_1'. The second fluid surrounds the lower layer and is set initially at constant height h_2. The initial configuration is schematically depicted in Fig. 7 with data summarized in Table 1.

Test	h_1 (m)	h_1' (m)	h_2 (m)	ρ_1 (kg.m^{-3})	ρ_2 (kg.m^{-3})
G	4	10	20	1000	1
H	10^{-6}	10	20	1000	1
I	4	10	20	1000	990
J	10^{-6}	10	20	1000	990
K	4	10	100	1000	990
L	10^{-6}	10	100	1000	990

Table 1: Initial conditions of the test problem analyzing the effects of the fluids' densities.

In all following tests, the gravity constant is set to $g = 10$ m.s^{-2} and the top of the Heaviside plateau is at $h_1' = 10$ m. The results are shown at time $t = 1$ s and computed on a 1000-cell

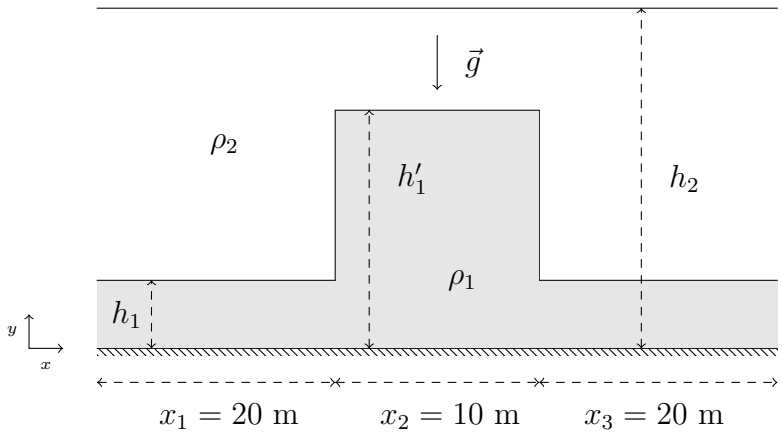

Figure 7: Schematic representation of the test problem analyzing the effects of the fluids' densities. A fluid layer with a Heaviside profile is set to motion under gravity effects and interacts with the lighter fluid initially above.

mesh with second order MUSCL-type scheme and $CFL = 0.5$. Figure 8 examines two different density ratios. Plots G and H consider $\rho_1 = 1000$ kg.m^{-3} and $\rho_2 = 1$ kg.m^{-3}, this situation being typical of water/air configurations while Plots I, J, K and L consider $\rho_1 = 1000$ kg.m^{-3} and $\rho_2 = 990$ kg.m^{-3}, a situation reminiscent of water/oil flows.

Besides, two different values of h_1 are used. The left column of Fig. 8 considers initially $h_1 = 4$ m while the right column uses $h_1 = 10^{-6}$ m. We will see that this initial data influences significantly computed results. All plots of Fig. 8 use $h_2 = 20$ m with the exception of Plots K and L that use a much larger height for the upper layer, $h_2 = 100$ m. This data also influences the results.

Small density ratio

When the density ratio is small, such as the situation of Fig. 8 G and H, considering a water/air-type configuration, the solutions of the two-layer system (2.3) are in excellent agreement with the exact solutions of the Saint-Venant model. For these two tests, $h_1' = 10$ m, $h_2 = 20$ m and $h_1 = 4$ m for Plot G and $h_1 = 10^{-6}$ m for Plot H.

In Plot G of Fig. 8, the Heaviside profile of the lower layer gives rise to four waves moving in each direction. The extreme waves steepen through compression waves into two shocks, while the back waves spread out as rarefaction waves.

However, the solution in Plot H of Fig. 8 is significantly different as the initial height of the lower-layer is as low as numerically acceptable (outside the Heaviside profile). Thereby the

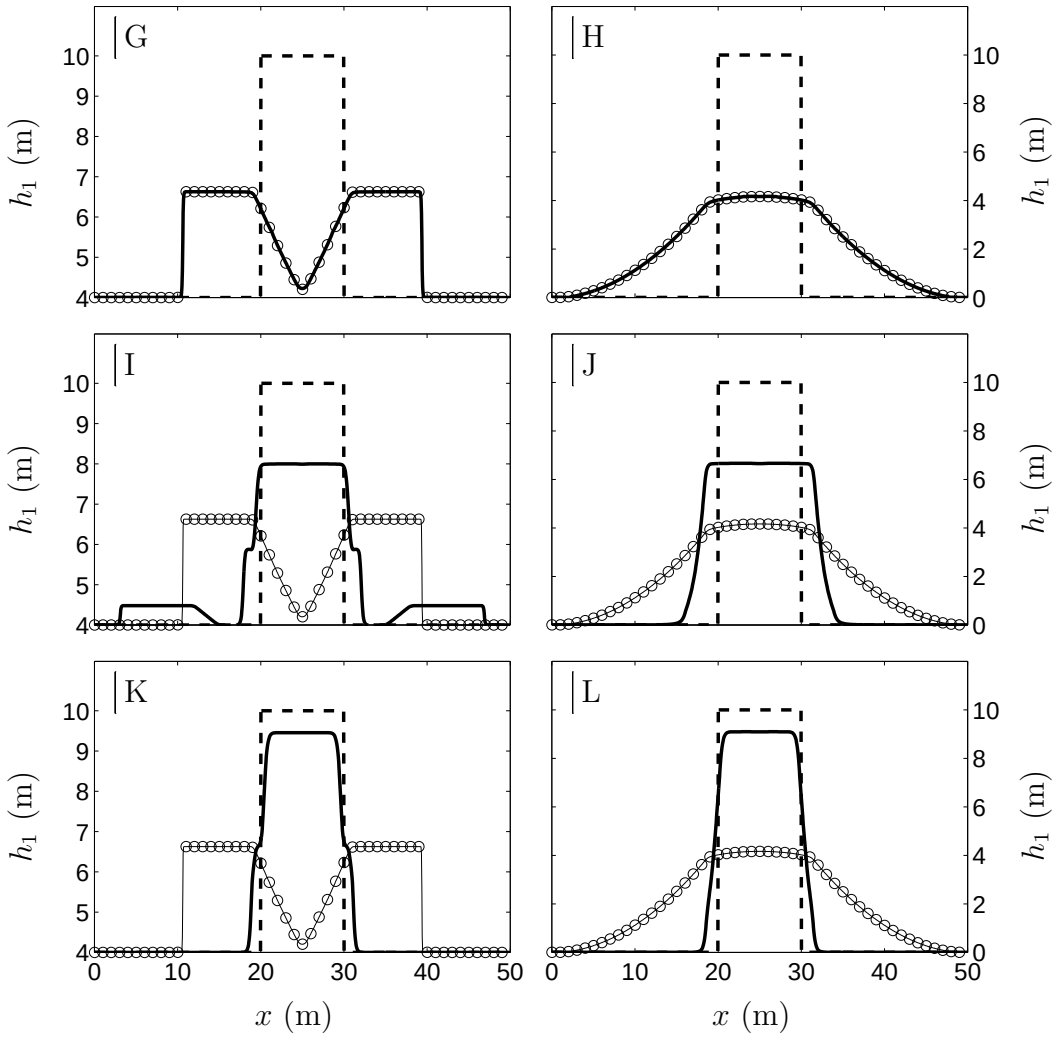

Figure 8: Comparison of the computed solutions with the present HLL-type Riemann solver (thick lines) for the two-layer model versus the exact solution of the one-layer Saint-Venant equations (thin lines and symbols). System (2.3) uses an artificial sound speed reading $c_k = \theta_k \sqrt{\frac{1}{2} g h_k}$ with $\theta_k = 2$. The dashed lines represent the initial conditions. Final time: $t \approx 1$ s. All results use a 1000-cell mesh. Second-order MUSCL-type numerical scheme is used with Sweeby's limiter ($\phi = 1.1$, see [22]) and $CFL = 0.5$. For the sake of clarity, 50 symbols are plotted for the exact solution of the single layer model. On the column at left, the initial height is $h_1 = 4$ m and on the column at right $h_1 = 10^{-6}$ m. When the density ratio ($r = \frac{\rho_2}{\rho_1}$) is small, as in configurations G and H, the two-layer and single-layer models are in perfect agreement. Large differences appear when the density ratio increases as shown in configurations I, J, K and L.

solution evolves continuously throughout the entire numerical domain as there is not enough fluid, regarding the lower-layer (h_1), to observe a compression process: expansion waves only are present.

Large density ratio

Plots I and J of Fig. 8 repeat the same test ($h'_1 = 10$ m, $h_2 = 20$ m, $h_1 = 4$ m (Plot I) and $h_1 = 10^{-6}$ m (Plot J)) but with a water/oil-type configuration. As expected, the solutions are different from the one-fluid solutions, as the two fluids are dense and interact each other, this interaction being taken into account by the two-fluid model only. The two-layer solutions are shown with full lines and the single-layer Saint-Venant solution is shown with symbols, just to compare the limit solutions.

The interaction of the two fluids influences significantly the computed results as an interesting wave structure appears in Plots I of Fig. 8. Right and left facing shock waves propagate faster than those of the single layer system. These shocks induce an increase of the fluid layer's height. They are followed by expansion waves that decrease these heights. Contact waves follow these expansion waves, followed by extra expansion waves that decrease the initial height h'_1.

The solution is quite different when $h_1 = 10^{-6}$ m initially (Plot J) where only two expansion waves are observable. The interaction of the two fluids influences the flow, as the first fluid moves more difficultly into the second one as a result of comparable densities.

Large upper-layer

Plots K and L of Fig. 8 keep on analyzing the present density ratio (water/oil) but with different height for the second fluid that is now set to $h_2 = 100$ m. Doing so, the domain is mainly filled with the upper layer and Plots K and L show that the first fluid moves into the second one difficultly. The difference of initial height for the first fluid $h_1 = 4$ m (Plot K) and $h_1 = 10^{-6}$ m (Plot L) is minor compared to the effect of the large layer of second fluid ($h_2 = 100$ m). As the entire domain is mainly filled with heavy fluids, the flow is slowly set to motion under gravity effects.

Concluding remarks

Those last results reveal that the two-fluid model (2.3) is able to recover the one-layer Saint-Venant system when the effects of the surrounding fluid are negligible, as expected. This behavior appears when the density ratio between the lightest fluid and the heaviest one is small.

They also reveal the importance of the two-layer model when the density ratio is arbitrary. Indeed, the two-layer system is able to deal with interactions between fluids unlike the conventional one-fluid Saint Venant model. Note that the previous tests have been computed with the HLL-type Riemann solver presented in Section 3.2, the VFRoe method being unable to keep positivity of the heights. Note also that drag effects are absent in these computations.

4.3. Comparison of VFRoe and HLL

The two solvers considered in the present paper are tested on a flow configuration examined in Abgrall and Karni (2009) [10]. The following tests set gravity constant to $g = 10$ m.s^{-2} and density ratio to $r = \frac{\rho_2}{\rho_1} = 0.98$. Hereby, $\rho_1 = 1200$ kg.m^{-3} and $\rho_2 = 1176$ kg.m^{-3} are used. Initially, different heights are present from either side of the initial discontinuity and results in the creation of a flow under gravity effects. The numerical domain is 1 m long and the initial discontinuity is located at $x = 0.5$ m. On the left of this discontinuity $h_1 = 0.5$ m and h_2= 0.5 m. On the right, $h_1 = 0.45$ m and $h_2 = 0.55$ m. The first order Godunov-type scheme is used with $CFL = 0.7$ in the following tests. Doing so, the comparison between solvers is free of extra ingredients, such as gradient limiters.

Figure 9 displays the results obtained with the HLL-type solver and the VFRoe method on a 100-cell mesh. The initial velocity is set to $u_1 = u_2 = 0$ m.s^{-1} throughout the entire domain. The results are shown at time $t \approx 0.12$ s.

The hyperbolic model (2.3) considers compressible fluids during the wave propagation stage. However, the pressure relaxation step restores incompressibility as shown in Fig 9 where the densities ρ_1 and ρ_2 remain constant. The numerical solutions consist in 4 waves emerging from the initial discontinuity. Both methods predict the same solution qualitatively, but the VFRoe solver produces spurious oscillations while the HLL one is monotonic.

As initially $u_1^{left} = u_1^{right} = u_2^{left} = u_2^{right} = 0$ m.s^{-1}, the velocity $\overline{u} = 0$ m.s^{-1} and the full state vector $\overline{W}$ in the VFRoe solver induces singularities in the eigenvectors' decomposition. To

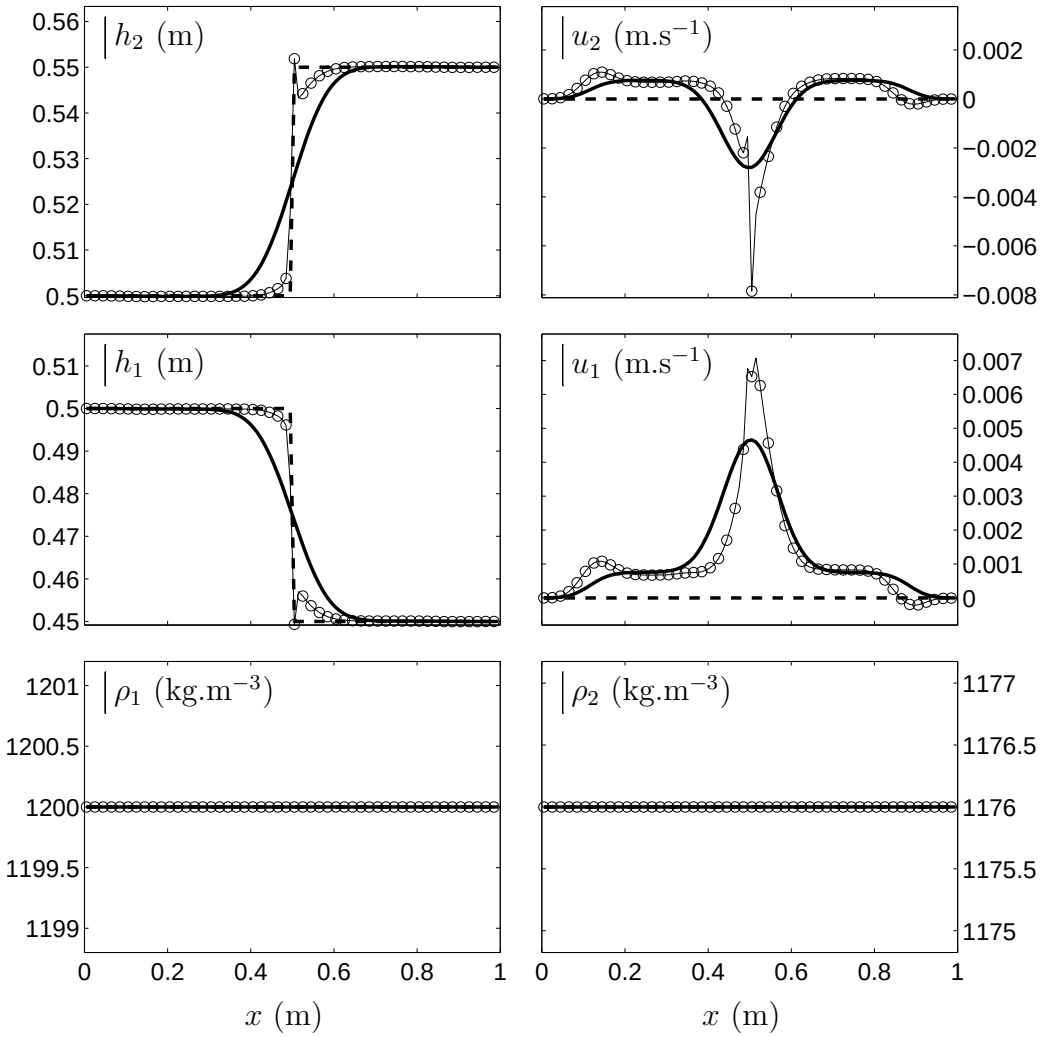

Figure 9: Comparison of the computed solutions with the present HLL-type Riemann solver (thick lines) versus the computed solutions with the VFRoe method (thin lines and symbols). The dashed lines represent the initial conditions: $h_1^{left} = 0.5$ m, $h_1^{right} = 0.55$ m, $u_1^{left} = u_1^{right} = 0$ m.s^{-1}, $\rho_1 = 1200$ kg.m^{-3}, $\rho_2 = 1176$ kg.m^{-3}. For the first fluid, the numerical parameter reads $\theta_1 = 3.5$, for the second fluid, $\theta_2 = 3$. These parameters are minimum values for successful computations with VFRoe. Final time: $t \approx 0.12$ s. First-order Godunov-type numerical scheme is used with $CFL = 0.7$ and 100 cells. For the sake of clarity, only 50 symbols out of 100 are plotted for the VFRoe method.

lower this effect, different sound speeds (through θ_1 and θ_2) have been considered in the various fluids. In the absence of such correction, the VFRoe solver fails immediately. Consequently, $\theta_1 \neq \theta_2$ is used as well with the HLL-type solver for proper comparison.

Figure 10 addresses the same test problem on a $10,000$-cell mesh, showing convergence to the same solution of both VFRoe and HLL. With refined mesh, the interfacial waves are clearly connected to a constant plateau spanning as time evolves. Besides the four-wave structure is clearly observable in the velocity plots.

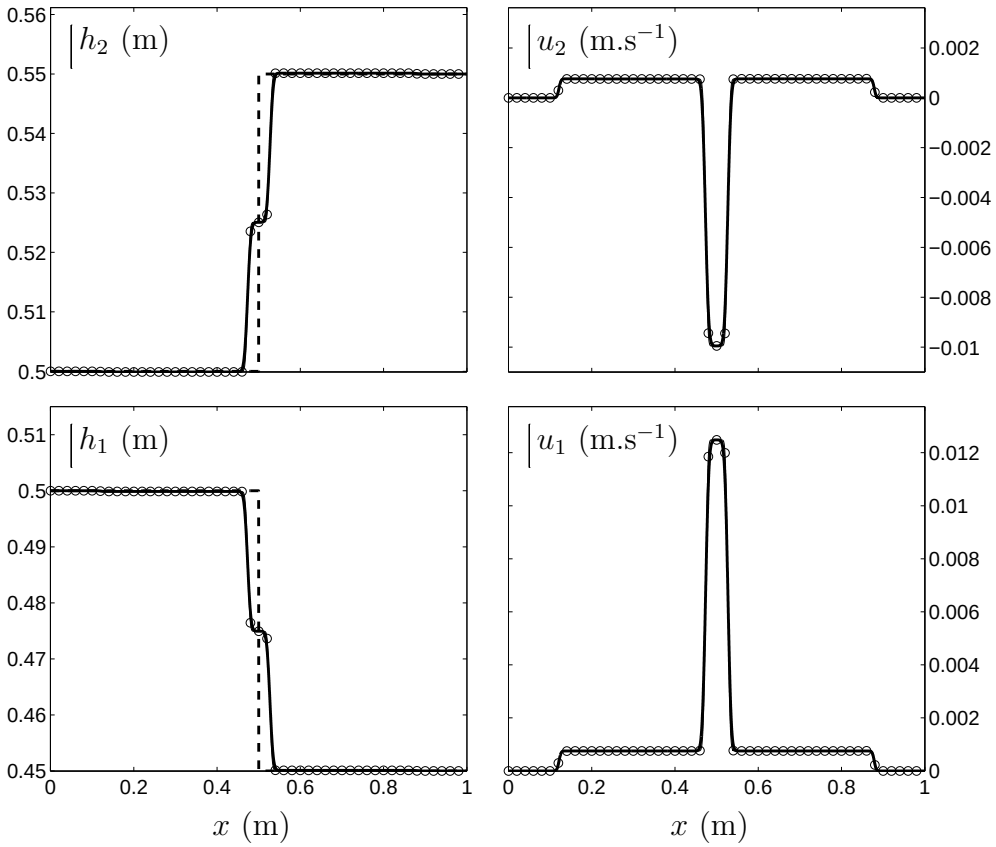

Figure 10: Comparison of the computed solutions with the present HLL-type Riemann solver (thick lines) versus the computed solutions with the VFRoe method (thin lines and symbols). The dashed lines represent the initial conditions: $h_1^{left} = 0.5$ m, $h_1^{right} = 0.55$ m, $u_1^{left} = u_1^{right} = 0$ m.s^{-1}, $\rho_1 = 1200$ kg.m^{-3}, $\rho_2 = 1176$ kg.m^{-3}. For the first fluid, the numerical parameter reads $\theta_1 = 3.5$, for the second fluid, $\theta_2 = 3$. Final time: $t \approx 0.12$ s. First-order Godunov-type numerical scheme is used with $CFL = 0.7$ and $10,000$ cells. For the sake of clarity, only 50 symbols out of $10,000$ are plotted for the VFRoe method. Both methods converge to the same solution.

The next test repeats the previous one with non-zero initial velocities. Those are set to $u_1 = u_2 = 2.5$ m.s^{-1} throughout the entire domain. This test was examined in Abgrall and

Karni (2009) [10] and computed with both 400 and 10, 000-cell meshes. The same grids are used here to compare the present model and HLL solver with the results given in [10]. Figure 11 shows the results at time $t \approx 0.07$ s with 400-cell mesh.

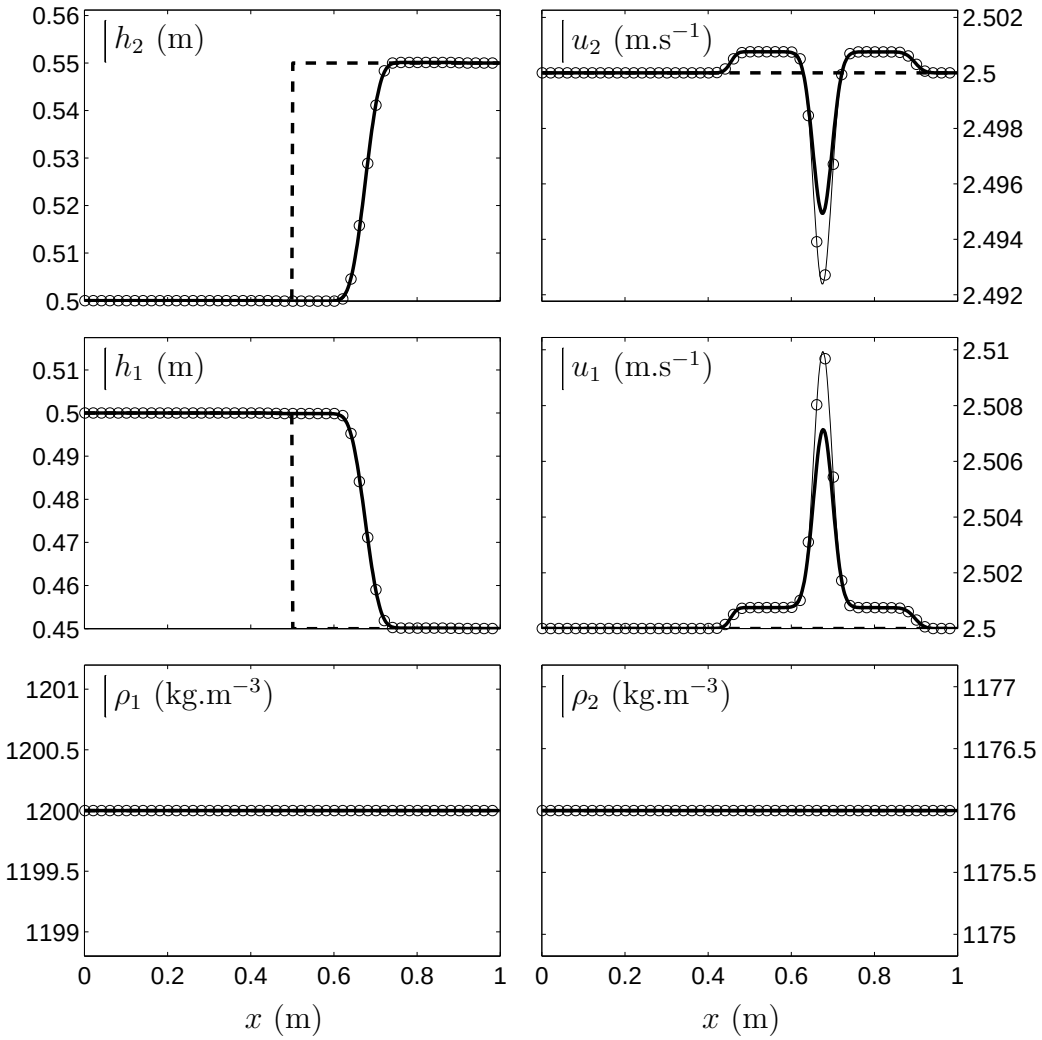

Figure 11: Comparison of the computed solutions with the present HLL-type Riemann solver (thick lines) versus the computed solutions with the VFRoe algorithm (thin lines and symbols). The dashed lines represent the initial conditions: $h_1^{left} = 0.5$ m, $h_1^{right} = 0.55$ m, $u_1^{left} = u_1^{right} = 2.5$ m.s^{-1}, $\rho_1 = 1200$ kg.m^{-3}, $\rho_2 = 1176$ kg.m^{-3}. For the first fluid, the numerical parameter reads $\theta_1 = 3.5$, for the second fluid, $\theta_2 = 3$. Final time: $t \approx 0.07$ s. First-order Godunov-type numerical scheme is used with $CFL = 0.7$ and 400 cells. For the sake of clarity, only 50 symbols out of 400 are plotted for the VFRoe method.

As a consequence of non-zero initial velocities and fine mesh resolution, computational conditions are easier for the VFRoe-type solver that does not oscillate. The expected behavior is recovered. The heights and velocity profiles are transported to the right and the effects of

gravity seen in Figs. 9 and 10 are still present. As expected the densities remain constant as a consequence of pressure relaxation. Figure 12 shows the results of the same test with $10,000$-cell mesh.

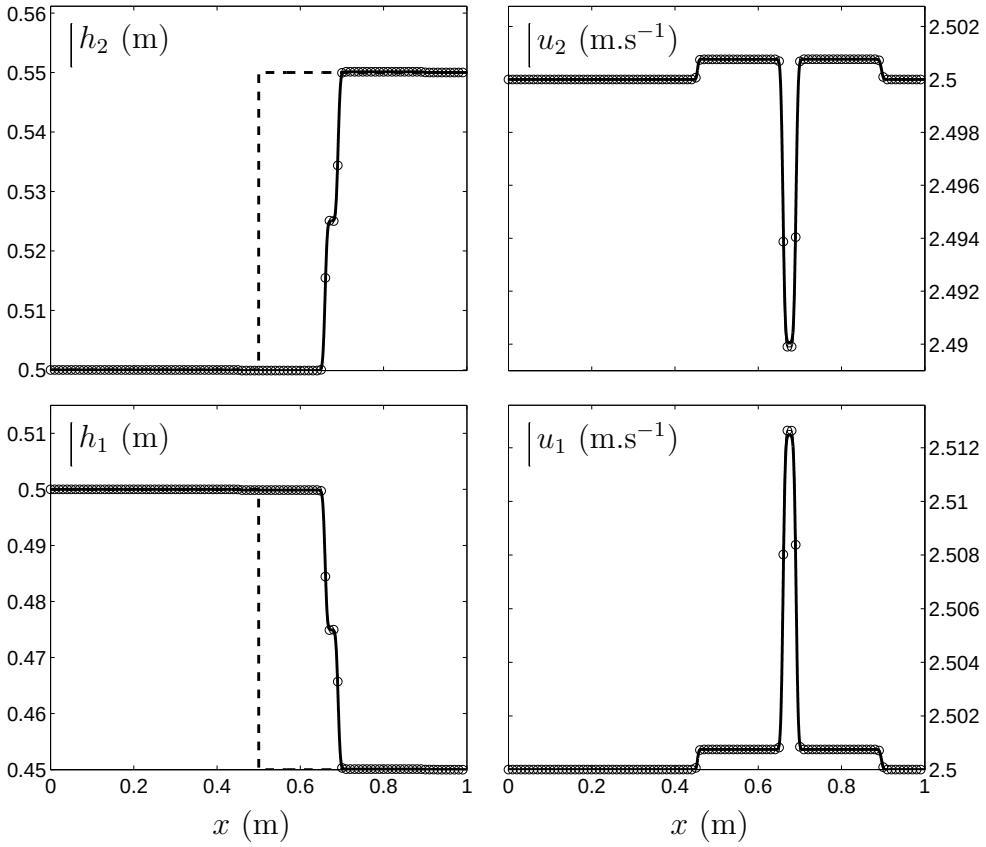

Figure 12: Comparison of the computed solutions with the present HLL-type Riemann solver (thick lines) versus the computed solutions with the VFRoe algorithm (thin lines and symbols). The dashed lines represent the initial conditions: $h_1^{left} = 0.5$ m, $h_1^{right} = 0.55$ m, $u_1^{left} = u_1^{right} = 2.5$ m.s^{-1}, $\rho_1 = 1200$ kg.m^{-3}, $\rho_2 = 1176$ kg.m^{-3}. For the first fluid, the numerical parameter reads $\theta_1 = 3.5$, for the second fluid, $\theta_2 = 3$. Final time: $t \approx 0.07$ s. First-order Godunov-type numerical scheme is used with $CFL = 0.7$ and $10,000$ cells. For the sake of clarity, only 100 symbols out of $10,000$ are plotted for the VFRoe method.

The HLL-type solver and the VFRoe-type method are in excellent agreement and are in excellent agreement with the results given in Abgrall and Karni (2009) [10] as well.

5. Comparison of two-layer shallow water versus two-dimensional two-fluid computations

The averaged (or homogenized) solution computed by the present one-dimensional two-layer shallow water system (2.3) is now compared to the solution of a multidimensional model involving

material interfaces. As mentioned in the introduction, the two-layer approach is expected to provide comparable results with considerable computational savings.

In the following, solutions computed with the compressible two-phase flow model of Saurel et al. (2009) [23] are used as reference solutions. This model is a pressure disequilibrium system which tends, in its asymptotic limit of stiff pressure relaxation, to the model of Kapila et al. (2001) [14], able to compute fluid interfaces as diffuse numerical zones. Interface sharpening can be achieved with the simple and efficient method of Chiapolino et al. (2017) [20].

To compare the solutions computed by both approaches (multidimensional interface model and one-dimensional two-layer shallow water one), the test configuration of Fig. 7 is used with $x_1 = 40$ m, $x_2 = 20$ m and $x_3 = 40$ m. Other associated data are summarized in Table 2.

Test	h_1 (m)	h_1' (m)	h_2 (m)	ρ_1 (kg.m^{-3})	ρ_2 (kg.m^{-3})	γ_1	γ_2
1D/2D	10^{-6}	1	10	3.506	1.29	1.67	1.4

Table 2: Initial conditions of the test problem to compare the multidimensional interface approach and the one-dimensional two-layer shallow water model. γ_k represents the thermodynamic polytropic coefficient of fluid k used in the compressible two-phase flow model as parameter of the ideal-gas equations of state.

Krypton and air are considered at rest and at atmospheric conditions initially. The flow is set to motion by the gravity acceleration $|g| = 10$ m.s^{-2} and consists of two ideal gases evolving at low Mach number. Due to symmetric boundary conditions, only half of the domain is computed with the multidimensional approach. This latter uses an unstructured mesh made of $510,000$ triangular elements with spatial discretization varying from about 1.5 cm in the zone of interest ($\cong 480,000$ elements located between $y = 0$ m and $y = 1$ m) to about 1 m in the upper far field. The numerical boundaries are considered as atmospheric outflows except for the left side (symmetric condition) and bottom one (flat ground) considered as walls.

The accurate resolution of interfaces in multidimensional computations is improved with a second-order numerical method. The MUSCL-type method with "Overbee" limiter at interfaces is used as detailed in [20]. The very same second-order method is used with the two-layer shallow water system, computed on a 1000-cell mesh with van Leer's limiter [21]. Non-reflecting boundary conditions are used for the shallow water computations.

Results are shown in Fig. 13 at times $t = 5$ s and $t = 8$ s. The computed averaged height and averaged velocity of the multidimensional simulation are determined by the integration on the two-dimensional numerical domain as,

$$h_1 = \int_0^{h_2} \alpha_1 dy, \tag{5.1}$$

and

$$u_x = \frac{\int_0^{h_2} (\alpha_1 \rho_1 u_x)\, dy}{\int_0^{h_2} (\alpha_1 \rho_1) dy}, \tag{5.2}$$

where α_1 denotes the volume fraction of krypton and u_x denotes the averaged velocity of the two-phase mixture in the x-axis direction. The one-fluid shallow water solution is shown as well in Fig. 13 for comparison.

As expected, the two-layer model provides better results than the one-fluid system. The density ratio $r = \frac{\rho_2}{\rho_1} = \frac{1.29}{3.506} \simeq 0.37$ being moderate, the interaction between the two fluids is meant to be significant. The results of the two-layer shallow water system present a large zone where the agreement with the two-dimensional simulation is very good. Beyond this zone, the results computed by the multidimensional interface model present oscillations. These oscillations are due to the presence of Kelvin-Helmholtz instabilities as seen for example in Fig. 14 showing the 2D results at time $t = 2$ s.

Indeed, the multidimensional solution involves hydrodynamic instabilities that cannot be accounted for with the present two-layer shallow water model. The overall qualitative behavior of the one-dimensional approach is correct but the krypton is spread too far ahead with the two-layer model.

To improve agreement between 1D and 2D computations, drag effects are added in the two-layer formulation. Pressure (or "acoustic") drag is considered only and is modeled through the

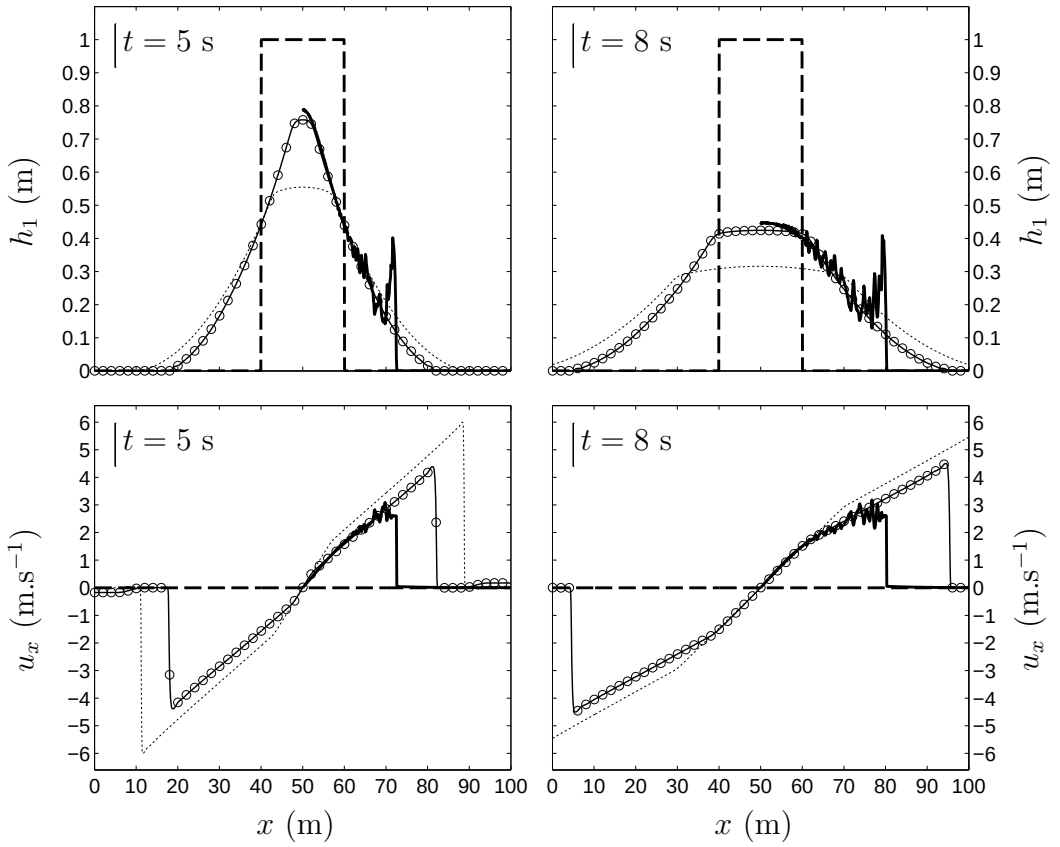

Figure 13: Comparison of the one-dimensional solution (thin lines and symbols) of the present two-layer shallow water model (HLL-type solver, $\theta = 2$) versus the two-dimensional computation of the diffuse interface model of Saurel et al. (2009) [23] (thick lines). The exact solution of the one-layer Saint-Venant equations is plotted (dotted lines) as well for comparison. The dashed lines represent the initial conditions. For the sake of clarity, 50 symbols are plotted for the two-layer solution. The column at left shows the results at time $t = 5$ s and the column at right shows the same results at time $t = 8$ s. For symmetric reasons, only half of the numerical domain is computed with the two-dimensional simulation. Both computations (two-layer and diffuse interface systems) use $CFL = 0.8$.

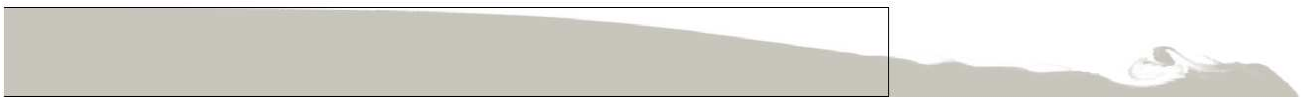

Figure 14: Kelvin-Helmholtz instabilities observed during the descent of krypton due to gravity effects, $g = -10$ m.s^{-2}. The figure presents krypton volume fraction contours. The black rectangle represents the initial position of the gas. The results are shown at time $t = 2$ s and are computed with the diffuse interface model of Saurel et al. (2009) [23] on an unstructured mesh made of $510,000$ triangular elements. MUSCL-type method is used with the "sharpening interface" method of Chiapolino et al. (2017) [20] and $CFL = 0.8$. For symmetric reasons, only half of the numerical domain is computed.

velocity relaxation terms that appear in the right-hand side of the momentum equations,

$$\begin{cases} \dfrac{\partial\left(h_1\rho_1u_1\right)}{\partial t}+\dfrac{\partial\left(h_1\rho_1u_1^2+h_1p_1(\rho_1)+\frac{1}{2}\rho_1gh_1^2+g\rho_2h_1h_2\right)}{\partial x}=\rho_2gh_2\dfrac{\partial h_1}{\partial x}+p_0\dfrac{\partial h_1}{\partial x}+\dfrac{Z_1Z_2}{Z_1+Z_2}A_I(u_2-u_1), \\ \dfrac{\partial\left(h_2\rho_2u_2\right)}{\partial t}+\dfrac{\partial\left(h_2\rho_2u_2^2+h_2p_2(\rho_2)+\frac{1}{2}\rho_2gh_2^2\right)}{\partial x}=-\rho_2gh_2\dfrac{\partial h_1}{\partial x}+p_0\dfrac{\partial h_2}{\partial x}-\dfrac{Z_1Z_2}{Z_1+Z_2}A_I(u_2-u_1). \end{cases} \tag{5.3}$$

$Z_k=\rho_kc_k$ denotes the acoustic impedance of fluid k and A_I denotes the specific interfacial area. This acoustic drag effect modeling was developed in Saurel et al. (2003) [6]. Let us mention that upon integration over height, as done in Eqs. (5.1) and (5.2), the specific interfacial area A_I becomes dimensionless.

As shown in Figs. 15 and 16, computed results are significantly improved when drag effects are considered. The two figures show the solutions with respectively $A_I=0.025$ and $A_I=0.01$.

Indeed, the overall solution presents very good agreement with the 2D simulation using the material-interface-two-phase flow model. The results show the ability of the new two-layer shallow water model to predict the spreading and dispersal of two gases evolving at low Mach number. The numerical advantages of this system are significant. In addition to its simple resolution through the HLL-type Riemann solver (Section 3.2), computational time saving is tremendous. For instance, the computation of the preceding test problem required about 30 hours for the two-dimensional simulation (computing only half of the domain) with a parallelized code (MPI) running on 64 cores, while the one-dimensional computation needed only a couple of seconds and a sequential implementation.

6. Conclusion

A pressure relaxation model with 6 equations has been built, especially devoted to two-layer shallow water flows. The mathematical structure of the new formulation is well-posed and results in a strictly hyperbolic model. The system considers weak compressibility of the fluids, which is responsible for its hyperbolic behavior, and is shown to tend to the conventional, but conditionally hyperbolic, two-layer shallow water model in the stiff pressure relaxation limit.

A simple, efficient and robust HLL-type Riemann solver has been derived to solve the cor-

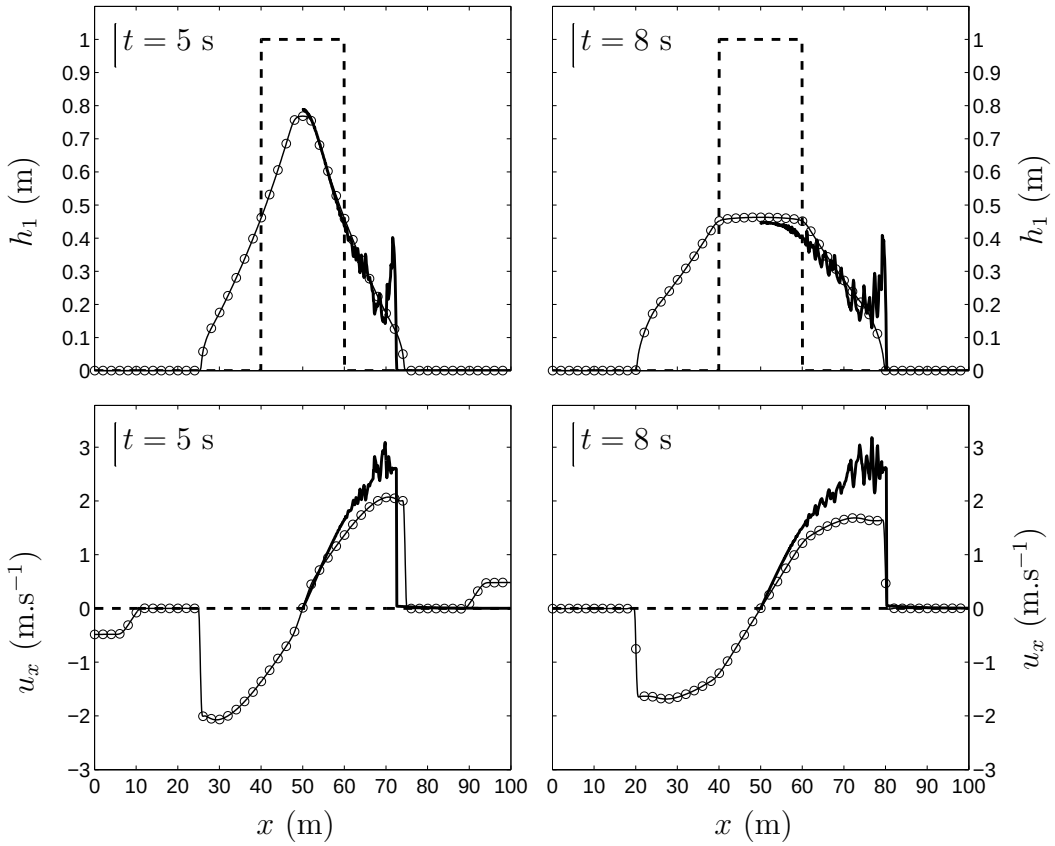

Figure 15: Comparison of the one-dimensional solution (thin lines and symbols) of the present two-layer shallow water model (HLL-type solver, $\theta = 2$) versus the two-dimensional computation of the diffuse interface model of Saurel et al. (2009) [23] (thick lines). Drag effects are included in the shallow water system with $A_I = 0.025$. For the sake of clarity, 50 symbols are plotted for the two-layer solution. The column at left shows the results at time $t = 5$ s and the column at right shows the same results at time $t = 8$ s. For symmetric reasons, only half of the numerical domain is computed with the two-dimensional simulation. Both computations (two-layer and diffuse interface systems) use $CFL = 0.8$.

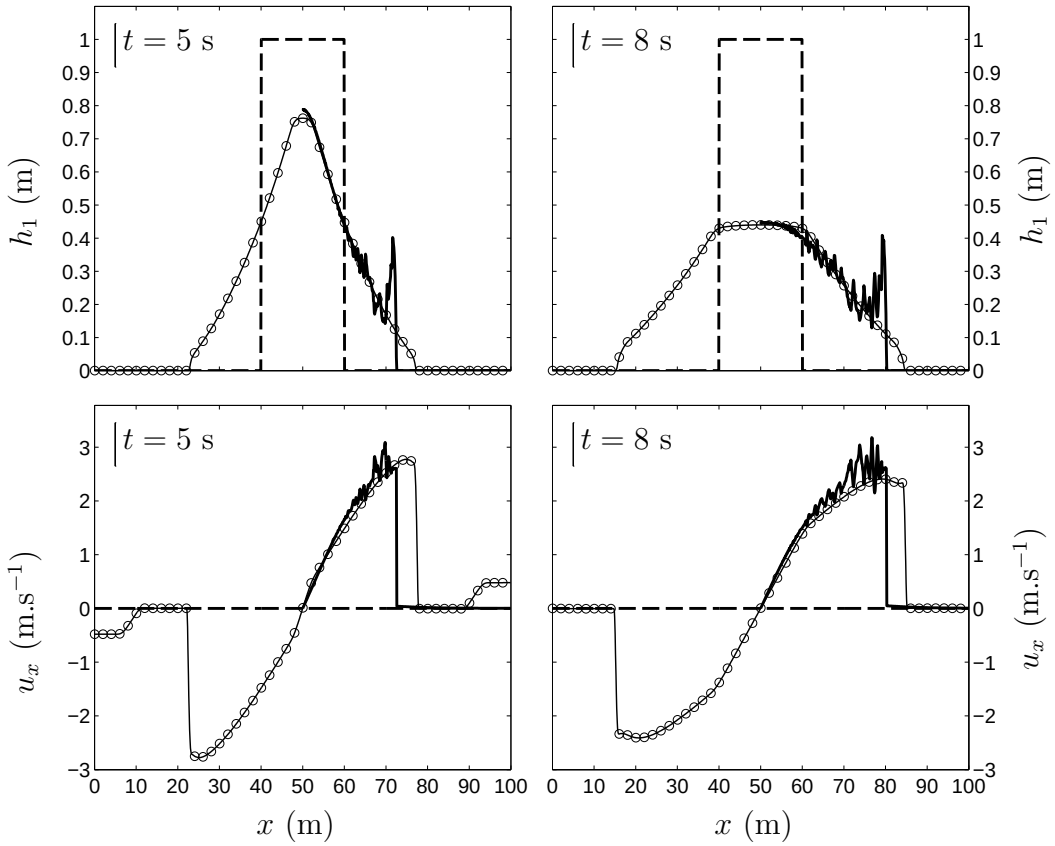

Figure 16: Comparison of the one-dimensional solution (thin lines and symbols) of the present two-layer shallow water model (HLL-type solver, $\theta = 2$) versus the two-dimensional computation of the diffuse interface model of Saurel et al. (2009) [23] (thick lines). Drag effects are included in the shallow water system with $A_I = 0.01$. For the sake of clarity, 50 symbols are plotted for the two-layer solution. The column at left shows the results at time $t = 5$ s and the column at right shows the same results at time $t = 8$ s. For symmetric reasons, only half of the numerical domain is computed with the two-dimensional simulation. Both computations (two-layer and diffuse interface systems) use $CFL = 0.8$.

responding non-conservative system. Computational examples have shown capabilities of the present formulation.

Compared to multi-D computations of gravity driven interfacial flows, the new model offers tremendous numerical advantages and computational savings. This is done to the price of a single parameter in the drag force model.

This research work can be continued in many directions. Among them, the consideration of variable topography, friction with the ground and interfacial area creation through turbulence modeling seem important.

Acknowledgements

The authors are very grateful to Jeaniffer Vides for participating in multiple valuable discussions that definitely helped to improve the quality of this work.

Part of this work has been carried out in the framework of the Labex MEC (ANR-10-LABX-0092) and of the A*MIDEX project (ANR-11-IDEX-0001-02) funded by ANR.

Support from CEA Gramat and especially Emmanuel Labedie are particularly Acknowledged.

References

[1] F. Marble, Dynamics of a gas containing small solid particles, Combustion and Propulsion (5th AGARD Colloquium) (1963) 175–213.

[2] M. Baer, J. Nunziato, A two-phase mixture theory for the deflagration-to-detonation transition (DDT) in reactive granular materials, International Journal of Multiphase Flow 12 (6) (1986) 861–889.

[3] R. Saurel, A. Chinnayya, Q. Carmouze, Modelling compressible dense and dilute two-phase flows, Physics of Fluids 29 (063301) (2017) doi: 10.1063/1.4985289.

[4] M. Lallemand, R. Saurel, Pressure relaxation procedures for multiphase compressible flows, Tech. rep., INRIA (2000).

[5] A. Forestier, J. Hérard, X. Louis, Solveur de type Godunov pour simuler les écoulements turbulents compressibles, Comptes Rendus de l'Académie des Sciences. Paris Série 1, Mathématique 324 (8) (1997) 919–926.

[6] R. Saurel, S. Gavrilyuk, F. Renaud, A multiphase model with internal degrees of freedom: Application to shock–bubble interaction, Journal of Fluid Mechanics 495 (2003) 283–321.

[7] D. Lhuillier, C. Chang, T. Theofanous, On the quest for a hyperbolic effective-field model of disperse flows, Journal of Fluid Mechanics 731 (2013) 184–194.

[8] G. Richard, S. Gavrilyuk, A new model of roll waves: comparison with Brock's experiments, Journal of Fluid Mechanics 698 (2012) 374–405.

[9] S. Gavrilyuk, V. Liapidevskii, A. Chesnokov, Spilling breakers in shallow water: Applications to Favre waves and to the shoaling and breaking of solitary waves, Journal of Fluid Mechanics 808 (2016) 441–468.

[10] R. Abgrall, S. Karni, Two-layer shallow water system: A relaxation approach, SIAM Journal on Scientific Computing 31 (3) (2009) 1603–1627.

[11] T. Gallouet, J. Masella, Un schéma de Godunov approché, Comptes Rendus de l'Académie des Sciences. Paris Série 1, Mathématique 323 (1) (1996) 77–84.

[12] L. Ovsyannikov, Two-layer shallow water model, Journal of Applied Mechanics and Technical Physics 20 (2) (1979) 127–135.

[13] R. Monjarret, Local well-posedness of the two-layer shallow water model with free surface, SIAM Journal on Applied Mathematics 75 (5) (2015) 2311–2332.

[14] A. Kapila, R. Menikoff, J. Bdzil, S. Son, D. Stewart, Two-phase modeling of deflagration-to-detonation transition in granular materials: Reduced equations, Physics of Fluids 13 (10) (2001) 3002–3024.

[15] R. Saurel, R. Abgrall, A multiphase Godunov method for compressible multifluid and multiphase flows, Journal of Computational Physics 150 (2) (1999) 425–467.

[16] A. Harten, P. Lax, B. Leer, On Upstream Differencing and Godunov-Type Schemes for Hyperbolic Conservation Laws, SIAM Review 25 (1) (1983) 35–61.

[17] R. LeVeque, Finite volume methods for hyperbolic problems, Vol. 31, Cambridge University Press, 2002.

[18] E. Toro, Riemann solvers and numerical methods for fluid dynamics: A practical introduction, Springer Science & Business Media, 2013.

[19] S. Davis, Simplified second-order Godunov-type methods, SIAM Journal on Scientific and Statistical Computing 9 (3) (1988) 445–473.

[20] A. Chiapolino, R. Saurel, B. Nkonga, Sharpening diffuse interfaces with compressible fluids on unstructured meshes, Journal of Computational Physics 340 (2017) 389–417.

[21] B. van Leer, Towards the ultimate conservative difference scheme. II. Monotonicity and conservation combined in a second-order scheme, Journal of Computational Physics 14 (4) (1974) 361–370.

[22] P. Sweby, High resolution schemes using flux limiters for hyperbolic conservation laws, SIAM Journal on Numerical Analysis 21 (5) (1984) 995–1011.

[23] R. Saurel, F. Petitpas, R. Berry, Simple and efficient relaxation methods for interfaces separating compressible fluids, cavitating flows and shocks in multiphase mixtures, Journal of Computational Physics 228 (5) (2009) 1678–1712.